

ARTICLE

Phase dependent encapsulation and release profile of ZIF-based biocomposites

Received 00th January 20xx,
Accepted 00th January 20xx

DOI: 10.1039/x0xx00000x

F. Carraro,^a M. de J. Velasquez-Hernandez,^a E. Astria,^a W. Liang,^b L. Twight,^a C. Parise,^{a,c,d} M. Ge,^e Z. Huang,^e R. Ricco,^a X. Zou,^e L. Villanova,^f C. Oliver Kappe,^c C. Doonan^{*b}, P. Falcaro^{*a,b}

Biocomposites composed of Zeolitic Imidazolate Frameworks (ZIFs) are generating significant interest due to their facile synthesis, and capacity to protect proteins from harsh environments. Here we systematically varied the composition (i.e. relative amounts of ligand (2-methylimidazole), metal precursor (Zn(OAc)₂·2H₂O, and protein) and post synthetic treatments (i.e. washes with water or water/ethanol) to prepare a series of protein@ZIF biocomposites. These data were used to construct two ternary phase diagrams that showed the synthesis conditions employed gave rise to five different phases including, for the first time, biocomposites based on the material, ZIF-CO3-1. We examined the influence of the different phases on two properties relevant to drug delivery applications: encapsulation efficiency and release profiles. The encapsulation efficiencies (of bovine serum albumin and insulin) were phase dependent and ranged from 75% to 100%. In addition, release profiles showed that 100% protein release varied between 40 and 300 minutes depending on the phase. This study provides a detailed compositional map for the targeted preparation of ZIF-based biocomposites of specific phases and a tool for the straightforward analysis of the crystalline phases of ZIF based materials (web application named “ZIF phase analysis”). These data will facilitate the progress of ZIF bio-composites in the fields of biomedicine and biotechnology.

Introduction

Metal-Organic Frameworks (MOFs) are a class of extended materials synthesized via a modular approach from inorganic (metal clusters or ions) and organic components that typically possess high surface areas and pore volumes.¹ By carefully selecting the framework building units and reaction conditions the chemistry, porosity and particle size of MOF can be precisely controlled. These properties have attracted researchers to explore MOFs, and their composites, for a wide variety of applications including biomedicine.² For example, MOF particles have shown unprecedented properties for the uptake and release of synthetic drugs,^{3,4} and more recently have been integrated with fragile biotherapeutics^{5,6} to improve their stability.^{7,8}

Recently, Zeolitic Imidazolate Frameworks (ZIFs)^{9,10} were used to encapsulate biomacromolecules and to form bio-active composites.^{11–16} The most explored ZIF material for the encapsulation of bioentities is ZIF-8 which is composed of Zn²⁺ cations and 2-methylimidazole (HmIM). ZIF-8-based biocomposites form spontaneously in water around negatively charged biomacromolecules without any additives.¹⁷ This specific process has been termed biomimetic mineralization due to its broad similarities to naturally occurring biomineralization.^{11,18,19} The ZIF matrix has been shown to protect fragile biomacromolecules and assemblies thereof (e.g. viruses and living cells) from conditions that typically lead to loss of their activity and also act as a vector for *in vitro* and *in vivo* delivery.^{11,12,15,19–23} With respect to drug delivery applications, the biomimetic mineralization approach yields high encapsulation efficiencies (EE%) for biomacromolecules, typically ranging from 80% to 100%.^{11,18,21} In general, high EE% values are relevant to drug delivery applications as the therapeutic is the valuable component of the composite.¹⁸ Release of the biomolecules is achieved *via* decomposition of the ZIF-8 matrix at pH values < 6.5, in the presence of chelating agents (e.g. ethylenediaminetetraacetic acid, EDTA), or in specific buffer solutions (e.g. phosphate-buffered saline, PBS).^{18,24,25}

ZIF-8 is a crystalline microporous material with sodalite (*sod*) topology that is synthesized by mixing aqueous solutions of HmIM and Zn²⁺.^{26–28} However, by varying the synthetic conditions, other topologies can be obtained (e.g. diamondoid (*dia*), katsenite (*kat*), ZIF-L).^{29–33} Similarly, for ZIF-based biocomposites, a variety of topologies can be accessed by

^a Institute of Physical and Theoretical Chemistry, Graz University of Technology, Stremayrgasse 9, Graz 8010, Austria

^b Department of Chemistry and the Centre for Advanced Nanomaterials, The University of Adelaide, Adelaide, South Australia 5005, Australia

^c Institute of Chemistry, University of Graz, NAWI Graz, Heinrichstrasse 28, 8010 Graz, Austria

^d Dipartimento di Chimica Industriale "Toso Montanari", Università di Bologna, Viale del Risorgimento 4, Bologna

^e Department of Materials and Environmental Chemistry, Stockholm University, 106 91 Stockholm, Sweden

^f Faculty of Technical Chemistry, Chemical and Process Engineering, Biotechnology, Graz University of Technology, Petersgasse 10-12, 8010 Graz, Austria

Electronic Supplementary Information (ESI) available: Experimental Section, Tables S1-6, Fig. S1-9, The “ZIF phase analysis” application description. See DOI: 10.1039/x0xx00000x

modulating the reaction conditions.^{19,34} In these studies, a fixed amount of biomacromolecule was employed while the concentrations of the ZIF components were varied. Thus, the network topology was controlled by the relative amount of ligand and cation. In a subsequent study we observed that increasing the biomolecule concentration (i.e. carbohydrates) and maintaining a fixed HmIM : Zn^{2+} ratio also led to a change in topology from *dia* to *sod*.¹⁸

This was most likely due to the dependence of sugar concentration on the pH of the reaction solution as the final solid ZIF product did not contain any carbohydrate. In addition to varying the relative concentration of the ZIF components and biomacromolecules, we have also found that post synthesis treatments (e.g. washing procedure) can trigger phase transitions.^{18,34}

Though the various ZIF topologies share the same chemical connectivity, they can exhibit vastly different physical and chemical properties. For example, ZIF (*sod*) has an accessible porosity of ca. $1800 \text{ m}^2 \text{ g}^{-1}$,²⁸ while ZIF (*dia*) is non porous to N_2 .³² In addition, each topology possesses a distinct density and surface chemistry which influences their chemical stability.^{35,36} Accordingly, for biomedical applications, such as drug delivery, we posit that the precise control of topology is critical for the design of a carrier with specific release profiles. In this present work, for the first time, we systematically explored how the combination of the ratio of ZIF components, biomolecule concentration and washing procedure determines the structural phase of the biocomposite.

Here, we screened 36 compositions varying the weight fractions

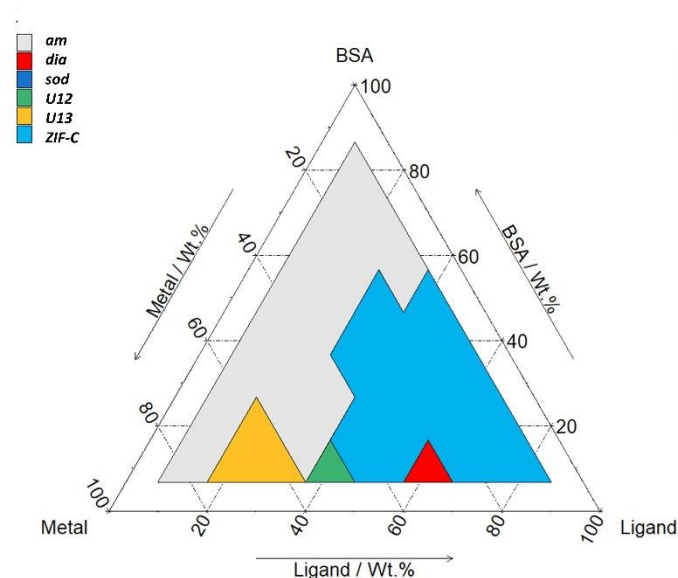
protein for the preparation of biocomposites.^{37–39} The washing procedure was carried out using either water only or water and ethanol. The resulting solids were analysed by X-ray diffraction (XRD) and their topologies represented in ternary phase diagrams namely *TD-H₂O* (water washed) and *TD-EtOH* (water and ethanol washed). A noteworthy result of this study is that we identified proteins encapsulated within ZIF- CO_3 -1, a ZIF previously obtained using solvothermal synthesis in absence of biomacromolecules.⁴⁰ For each distinct phase: amorphous, U13, sodalite, diamondoid, and ZIF- CO_3 -1 (here referred as *am*, *U13*, *sod*, *dia* and *ZIF-C*, respectively) we selected and characterized a representative sample using scanning electron microscopy (SEM), vibrational spectroscopy (Fourier Transformed Infrared, FTIR and Raman), and energy-dispersive X-ray spectroscopy (EDX).

Given the potential application of these biocomposites to drug delivery, for each identified phase we determined the encapsulation and release profiles of BSA and insulin (a clinical bio-therapeutic). Our results show that each of the biocomposites have high encapsulation efficiencies EE% and distinct release profiles. These data will inform and facilitate future research in the burgeoning area of MOF-based drug delivery.

Results and discussion

We prepared 36 different samples by varying the composition of zinc acetate, HmIM and BSA (each restricted to a mass

a Ternary Phase Diagram Water (*TD-H₂O*)



b Ternary Phase Diagram Ethanol (*TD-EtOH*)

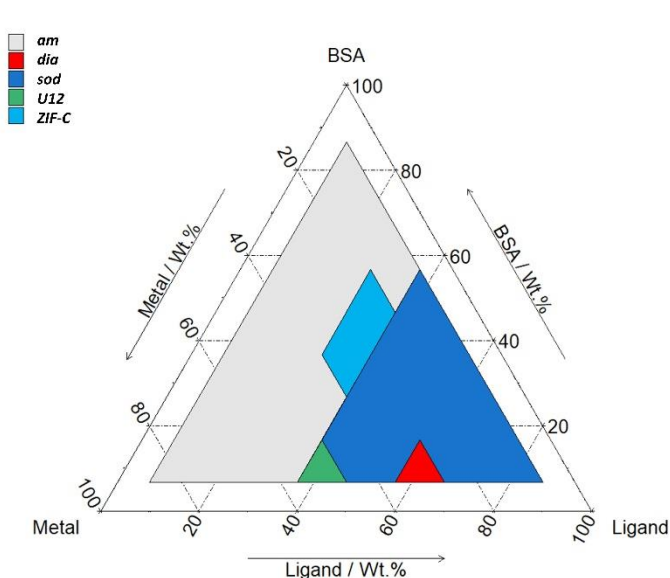


Figure 1: Ternary diagrams (by weight fraction, see Table S1 for details) of BSA, HmIM (labelled as Ligand) and $\text{Zn}(\text{OAc})_2 \cdot 2\text{H}_2\text{O}$ (labelled as Metal). *TD-H₂O* (a) represents the main phases (>50% wt, see Table S2 for details) obtained by washing the sample with DI water. *TD-EtOH* (b) represents the main phases (>50% wt, see Table S3 for details) obtained by washing the sample first with DI water and then with ethanol. The total mass of the reagent was chosen selecting a value in between those previous reported in the literature (see ESI† for further details).^{11,34}

of HmIM, $\text{Zn}(\text{OAc})_2 \cdot 2\text{H}_2\text{O}$, and Bovine Serum Albumin (BSA). BSA was selected as a model biomacromolecule since it has been widely employed in the literature as a standard, inexpensive,

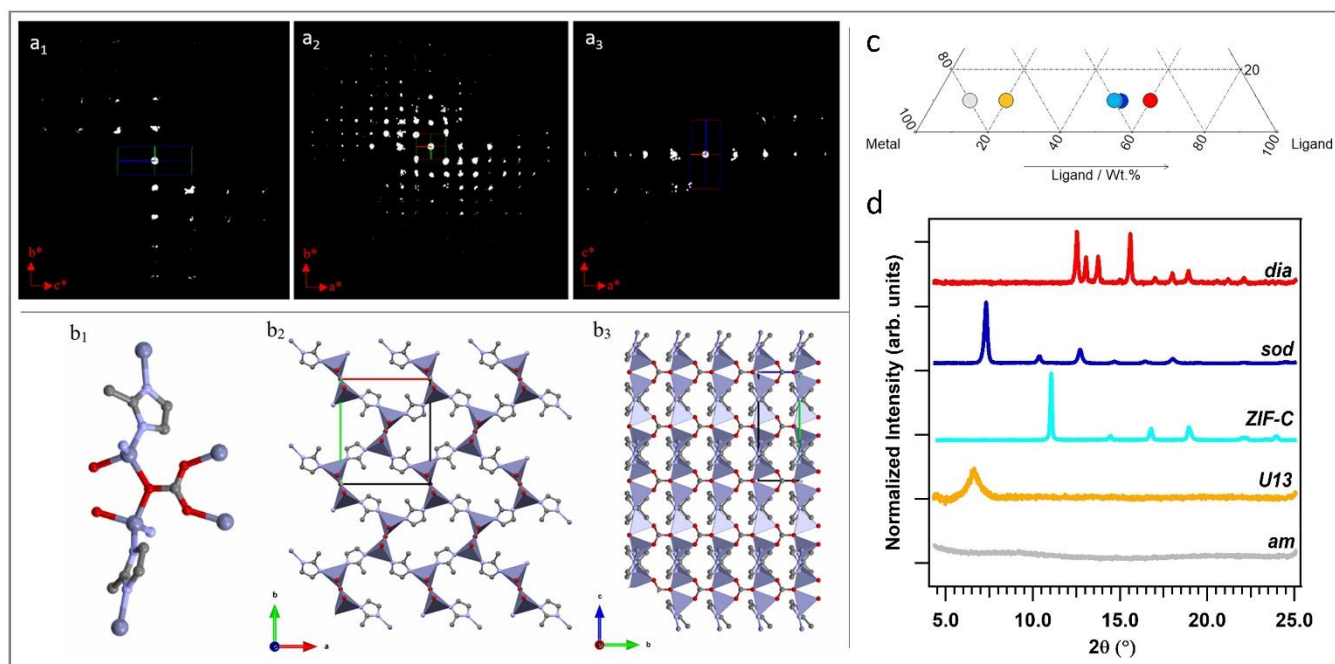


Figure 2: 2D slice cuts from the reconstructed 3D reciprocal lattice show the 0kl (a_1) $hk0$ (a_2) and $h0l$ (a_3) planes. The scattering background (see Fig. S2) was removed for clarification. Structure of ZIF-CO3-1: (b_1) coordination mode of Zn; (b_2) framework viewed along the c axis; (b_3) framework structure viewed along the a axis. The Zn, O, N and C atoms are shown in blue, red, light blue and grey, respectively. c) Section of the ternary diagram to highlight the samples selected as representative of the different phases (grey spot: amorphous biocomposite (TD-H₂O); yellow spot: **U13** (TD-H₂O); azure: **ZIF-C** (TD-H₂O); blue: **sod** (TD-EtOH); red: **dia** (TD-EtOH)). The **ZIF-C** and **sod** samples were obtained with the same protocol, but with different washing procedures (TD-H₂O and TD-EtOH, respectively). d) XRD patterns of the amorphous biocomposite and of the biocomposites with **dia**, **sod**, **ZIF-C** topologies, and **U13**.

fraction range of 10–80%, see Fig. S1 and Tab. S1 in ESI[†]) in a fixed volume of water (2 mL, see ESI[†] for experimental details) and examined their topology via XRD.

To explore the entire space of the variables, we selected compositions that were equally distributed within the phase diagram plot (see Fig. S1 in ESI[†]).

After mixing, the different solutions were left to stand at room temperature for 24 h. From each of the 36 vials, the solid was separated via centrifugation and divided in two parts. One part was washed with deionized (DI) water only and the other was washed with water and ethanol. The samples were then air dried and investigated by X-ray diffraction (XRD). The resultant phases are reported in the ternary diagrams that relate each polymorph to the relative composition of Zn(OAc)₂, HmIM, and BSA in the synthesis solution. Fig. 1a and b show the ternary diagrams of the samples washed with DI water (TD-H₂O) and with DI water and ethanol (TD-EtOH), respectively. Specific details related to the washing procedures and measurement conditions are reported in ESI[†].

When powders were washed only with DI water (TD-H₂O) we observed the formation of an amorphous product (**am**) for small mass fractions of HmIM (10–20%). However, increasing HmIM to 20–30% while keeping BSA ≤ 20%, we found crystalline patterns dominated by a phase we have previously identified as **U13**.³⁴ Moving towards lower mass fractions of Zn²⁺ (10%), we measured amorphous diffraction patterns until BSA exceeded 50%. The remaining mass fraction ratios yielded diffraction patterns attributed to **ZIF-C** (Fig. 1a and Fig. S1, Tab. S2 in ESI[†]). This was confirmed by applying continuous rotation electron

diffraction (cRED) technique (Fig. 2a, see ESI[†] for further details), which is a specialized technique for the structural determination of nanocrystals.^{41,42} **ZIF-C** is a high density framework (Fig. 2b) non porous to N₂ (see Fig. S3, ESI[†]), that is prepared using solvothermal conditions (DMF/H₂O, 140 °C)⁴⁰ and not observed as a component of a biocomposites until this work. In a limited number of samples, **ZIF-C** was found mixed with previously reported patterns termed **U12**, **U13**, and **dia** topology.³⁴

The TD-EtOH diagram indicates that ethanol washing gives rise to phase transitions: **U13** is no longer present and all the other samples with ZIF-C are partially or totally converted into **sod**, with the exception of the **dia/ZIF-C** mixed phase (TD-H₂O BSA/HmIM/Zn²⁺ = 10%/60%/30%) that transforms into **dia**. Furthermore, **U12** is converted to a mixture of 3 phases (**U12**, **sod**, **ZIF-C**). Lastly, for all samples with mass fraction = 10% of Zn²⁺ and HmIM ≥ 40% we measured pure **sod**. We observed diffraction patterns (i.e. crystalline) only for ca. wt_{HmIM} ≥ 30%, thus TD-EtOH confirms the important role of HmIM for the preparation of a crystalline material.

Combined TD-H₂O and TD-EtOH show the presence of 5 different phases (**am**, **sod**, **dia**, **U13**, **ZIF-C**) in their pure form or as compositions of phases (see Tables S2, S3 ESI[†]). It is well known that the physical and chemical properties of ZIFs are dependent on their phase^{32,43,44}, thus we were motivated to examine the biomolecule encapsulation and release profiles of each biocomposite. However, first, we characterised each material by XRD, FTIR and Raman Spectroscopies, their elemental distribution via EDX and morphologies by SEM. In

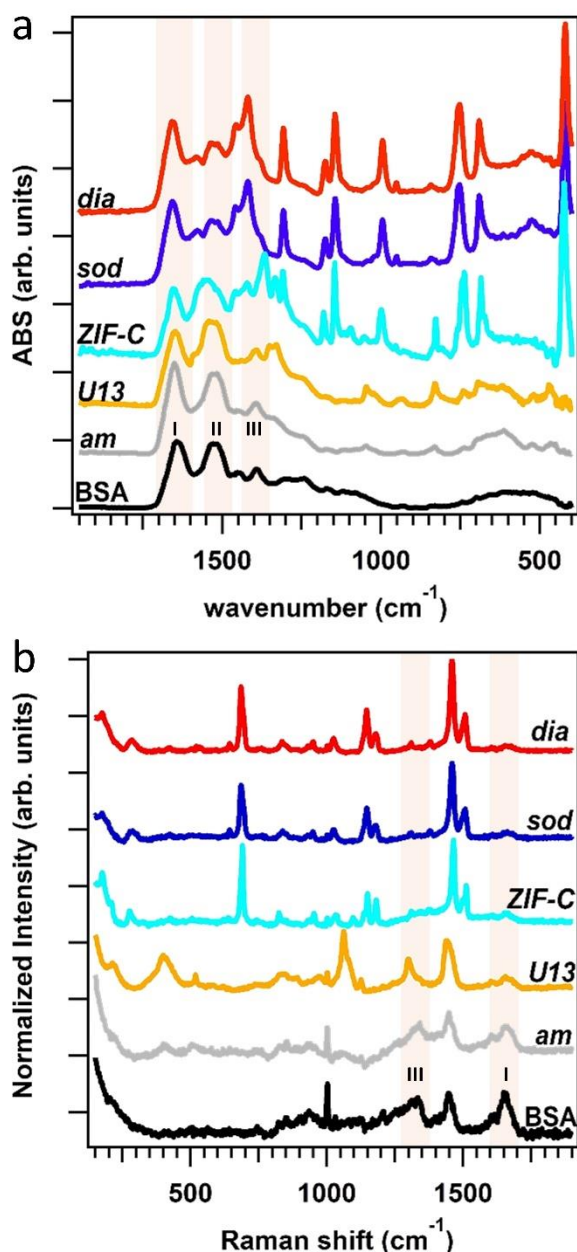


Figure 3: FTIR (a) and Raman (b) spectra of BSA, of the biocomposites with *am*, *dia*, *sod*, *U13* and *ZIF-C* phases. The spectral regions of Amide I, II and III bands of BSA are highlighted in light pink.

addition, given that biopharmaceuticals are the most expensive component of a drug delivery system^{45–47} we selected a biocomposite with a fixed 10 wt% of protein. Moving along this mass fraction we prepared the 5 different phases shown in Fig. 2c. The diffraction patterns plotted in Fig. 2d are univocally assigned to *dia*, *sod*, *ZIF-C* and *U13* (see Fig. S4, ESI[†]). For *am* the disordered state is confirmed by the absence of reflections. To facilitate the progress of $\text{Zn}(\text{mIM})_2$ bio-composites towards biomedicine and biotechnology, we have developed a web application (<https://rapps.tugraz.at/apps/porousbiotech/ZIFphaseanalysis/>) named *ZIF phase analysis*. By uploading diffraction patterns collected using $\text{Cu K}\alpha$ radiation, this web application allows for

1) a rapid identification of the crystalline phases, and 2) a rough estimation of the relative amounts (wt %). The web application was developed using the statistical software R – shiny package.⁴⁸ Additional information can be found in ESI[†].

To assess the connectivity and chemical composition of the bio-composites, we examined powder samples of *am*, *dia*, *sod*, *U13* and *ZIF-C* phases using vibrational spectroscopy (Fig. 3). Analysis of the FTIR data confirms the presence of characteristic modes of the peptide backbone of BSA such as the Amide I ($1700\text{--}1610\text{ cm}^{-1}$) and Amide II ($1595\text{--}1480\text{ cm}^{-1}$) bands.^{49,50} The spectra of *am* and *U13* did not show vibrational modes that could be attributed to the imidazolate ligand. Furthermore, the vibrational mode at ca. 420 cm^{-1} , assigned to the $\text{Zn}\text{--}\text{N}$ stretching mode, is missing in the selected *am* and *U13* samples. This confirms that *am* and *U13* are not $\text{Zn}(\text{mIM})_2$ -based polymorphs. Conversely, the spectra of *sod*, *dia* and *ZIF-C* show several bands ($420, 690, 752, 998, 1145, 1175, 1308, 1419, 1458, 1580\text{ cm}^{-1}$) typically observed for *sod*- $\text{Zn}(\text{mIM})_2$.^{31,34,51} The spectrum of *ZIF-C* shows additional bands in the $700\text{--}850$ and $1300\text{--}1400\text{ cm}^{-1}$ regions that can be assigned to bending and asymmetric stretching modes of CO_3^{2-} .⁴⁰ Moreover, the $\text{Zn}\text{--}\text{N}$ stretching mode is slightly shifted from 421 to 427 cm^{-1} ; we posit this is due to the different $\text{Zn}\text{--}\text{mIM}$ coordination environment with respect to *sod* or *dia* topologies. The Raman spectra ($160\text{--}1800\text{ cm}^{-1}$) of the same samples are reported in Fig. 3b. The *sod* and *dia* topologies show the typical Raman fingerprint of *sod*.^{52,53} For both *sod* and *dia*, the main bands are assigned to methyl bending (1459 cm^{-1}), C5-N stretching (1147 cm^{-1}), imidazole ring puckering (690 cm^{-1}) and $\text{Zn}\text{--}\text{N}$ stretching

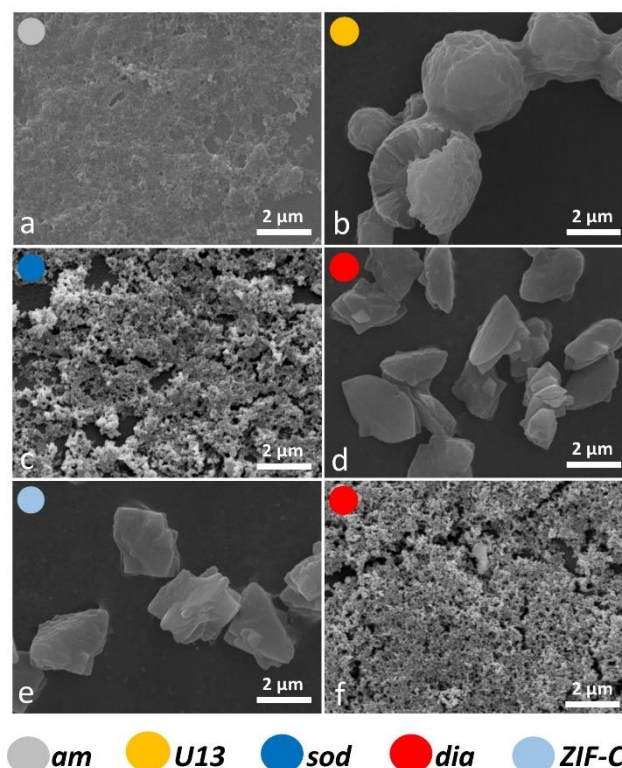


Figure 4: SEM micrographs of the biocomposites with *am* (a) and *U13* (b, from TD-H₂O), *sod* (c, from TD-EtOH), *dia* (from TD-H₂O (d) and from TD-EtOH (f)) and *ZIF-C* (e, from TD-H₂O) phases. *ZIF-C* refers to *ZIF-CO₃-1*.⁴⁰

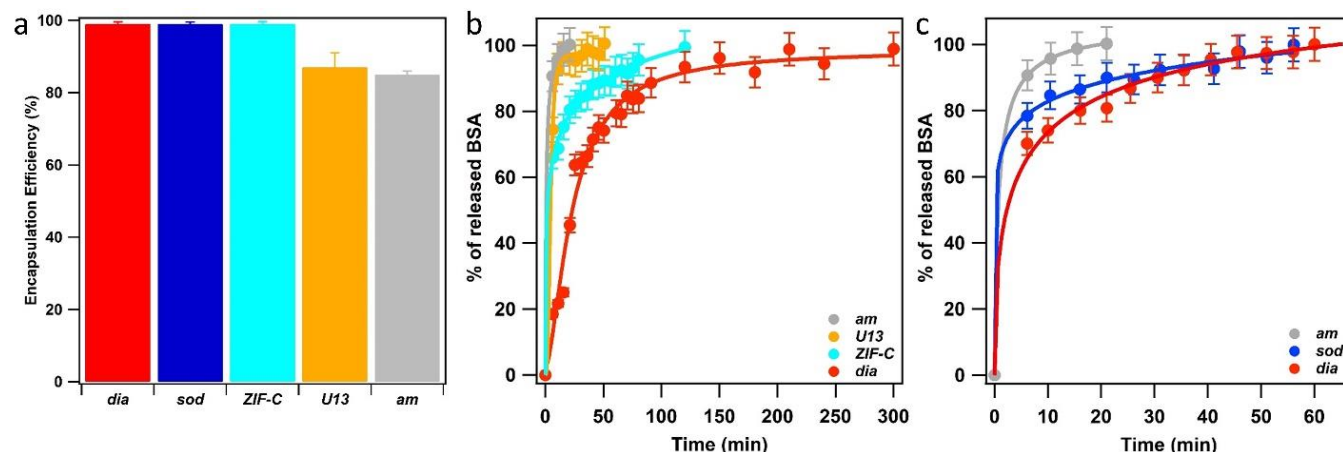


Figure 5: BSA EE% (a) and BSA release profiles (from TD-H₂O (b) and from TD-EtOH (c)) of the biocomposites with *am*, *U13*, *sod*, *dia* and *ZIF-C* phases. *ZIF-C* refers to ZIF-CO₃-1.⁴⁰

(178 and 278 cm⁻¹).^{52,53} Comparing the Raman spectra of *ZIF-C* to *sod*, small differences can be observed at 1466 cm⁻¹ (assigned to imidazole ring puckering and to methyl bending) and 1097 cm⁻¹ (assigned to CO₃²⁻ stretching mode).^{52–54} These data support the different Zn-mIM coordination environment. In all the three crystalline Zn(mIM)₂ phases (*sod*, *dia*, *ZIF-C*) we could confirm the presence of BSA (1550–1720 cm⁻¹, Amide I).⁵⁵ For amorphous and *U13* the vibrational modes of BSA dominate the spectra with broad bands assigned to Amide I (1600–1700 cm⁻¹), Amide III (1300–1350 cm⁻¹) and -CH deformation (1445 cm⁻¹).⁵⁵ The broad band at 400 cm⁻¹ could be attributed to Zn-O stretching. This indicates potential for zinc protein interactions.⁵⁶ The elemental composition of the biocomposites estimated by EDX shows a Zn content of ca. 5 wt% in the case of *sod*. This value increases to ca. 15% for *am* and ca. 18% for *U13* (details can be found in ESI†, Fig. S5 and Table S5), suggesting that *am* and *U13* are mainly composed of Zn and BSA. We note that Zn cations and BSA have been shown to form solid particles.^{57,58} Next, we investigated the morphology of the different phases by SEM (Fig. 4). For the water washed samples, very small particles of indistinguishable morphology were observed for *am* (Fig. 4a). While for *U13* the

image shows spherical particles, and for *dia*-Zn(mIM)₂ and *ZIF-C* aggregates of plates 2–3 μm in size (Fig. 4b and 4d and e, respectively). For the ethanol washed sample, the particle size was reduced to less than 100 nm (Fig. 4c, f and S6, ESI†), with the exception of *U13*. In this case, a similar particle morphology is observed despite the phase transition to *am* (Fig. S7, ESI†).

We then turned our efforts to investigate the potential of using the 5 biocomposites *am*, *U13*, *sod*, *dia*, and *ZIF-C* as drug delivery systems. Initially BSA was employed as a model bio-therapeutic.^{59,60} For each sample a 10% mass fraction of BSA was employed in the synthesis (*vide supra*) and two important properties of a drug carrier were assessed: EE% and release profile.^{61–63} The estimated EE% (average of five independent analyses) for the different phases is shown in Fig. 5a. For each phase, high EE% values were observed (EE% > 85%) and, remarkably, *dia*, *sod* and *ZIF-C* topology showed a 100% EE. Details can be found in ESI†.

BSA release profiles were investigated to ascertain the quantity of protein released over time. The dissolution of each biocomposite was performed by exposing 1.08 mg of each phase to citric acid buffer solution (1 mL, 100 mM, pH 5.5, room

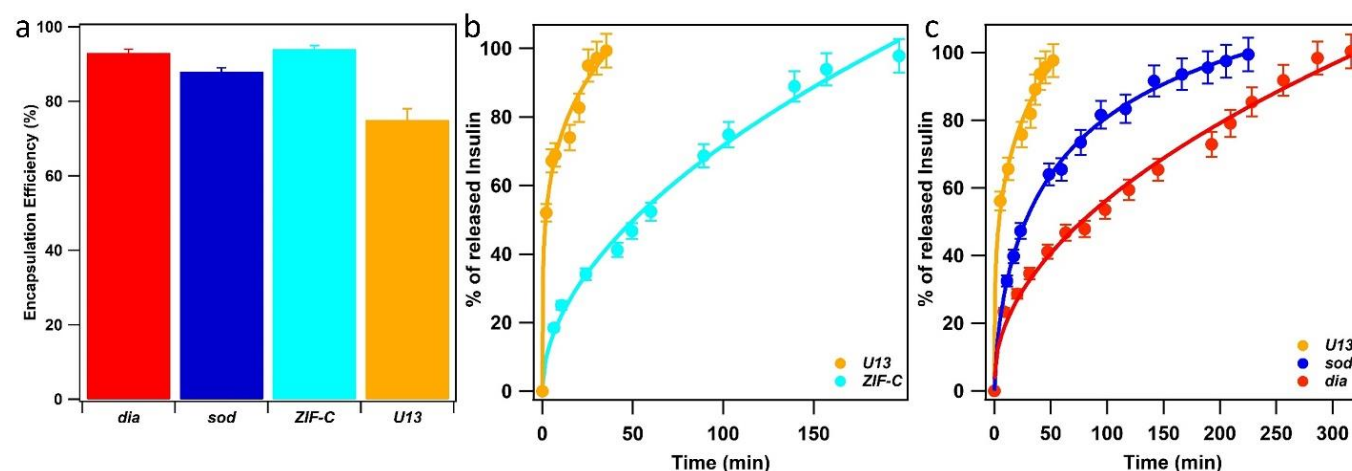


Figure 6: Insulin EE% (a) and Insulin release profiles of the biocomposites with *U13* and *ZIF-C* phases (b, water washed samples) and *U13*, *sod* and *dia* (c, EtOH washed samples) phases. *ZIF-C* refers to ZIF-CO₃-1.⁴⁰

temperature). We used UV-Vis and the Bradford Assay (see ESI† for further details) to measure the amount of BSA in solution over time (see ESI† for details), and the release profiles are plotted in Fig. 5b and c. The experimental data points were fitted with a logistic fitting function⁶⁴ which has previously been employed in the literature for the analysis of data related to the dissolution of different hydrophobic carries, including ZIF-8.^{18,65,66} Among the biocomposites washed only with water, **am** and **U13** showed the fastest dissolution: in 20 minutes, 100% of the encapsulated BSA was released (see ESI†) and the slowest release was measured for the **dia** topology: 100% of protein release was reached after 250 minutes. Whilst **ZIF-C** released 100% of the protein in 120 min. With respect to the ethanol-washed samples, **am** showed the rapid release ca. 20 min and similar to the water washed samples the slowest release was measured for the biocomposite of **dia** topology. However, in this case the release was significantly faster; 100% was observed in 60 minutes (compared to 250 min for the water washed samples). Given that the topologies are identical for the water and ethanol washed samples we posit that difference in release times is due to the significantly smaller particle size of the ethanol-washed **dia** biocomposites (100 nm) compared to the water-washed particles (2 μ m). Thus, we can conclude that both the crystalline phase and the particle size play a crucial role in the design of MOF carriers for drug delivery applications.

To explore the potential biomedical applications of these biocomposites for the delivery of therapeutics we determined the release profiles of insulin encapsulated within the same 5 phases as studied for BSA. XRD data confirmed the expected phases (see Fig. S8, ESI†). However, for the **dia** phase an impurity of **sod** was present (15 wt%). For the samples with **dia**, **sod** and **ZIF-C** topology we measured 93, 88 and 94% of insulin EE%, respectively (Fig. 6a). The lowest value was found for **U13** sample (EE%=75%). Then, we tested the insulin release profiles (Fig. 6b and c). Among the crystalline water-washed samples, the **U13** biocomposite showed the fastest release: in the first 40 minutes 100% of the encapsulated insulin was released. The slowest release was measured for the sample that possesses **ZIF-C** topology: the insulin release is 50% in 60 min and 100% in 200 min. Among the ethanol-washed crystalline samples, **U13** showed the fastest release and a profile comparable to the water-washed **U13** sample. The slowest release was measured for the sample that possesses **dia** topology: 100% of release was reached in 300 minutes. The sample that possesses **sod** topology showed an intermediate release profile (100% of insulin released in 220 minutes).

Conclusion

We investigated the dependence of the crystal phases on the mass fraction of precursors (BSA or insulin, $\text{Zn}(\text{OAc})_2 \cdot 2\text{H}_2\text{O}$, HmIM) and the washing procedure (water or ethanol). For BSA we prepared 36 samples, washed only with water; the crystal phases were used to plot a ternary phase diagram (TD- H_2O). More than 40% of the samples were found to be amorphous and the remaining samples were crystalline and non-porous

(**dia**, **U13**, **ZIF-C**). Then, we tested the effect of ethanol washes on the 36 samples and found that it gave rise to phase transitions. For example, **U13** became amorphous, while **ZIF-C** transformed partially or completely into **sod**. From these data we constructed a new second ternary phase diagram (TD-EtOH). Approximately 50% of the samples in TD-EtOH are amorphous; the remaining crystalline samples are dominated by the porous **sod** topology. The two ternary diagrams were used for the design of BSA-based composites with different crystallinity: starting with the same amount of protein, we could select conditions for the preparation of 5 different crystalline phases. To assess the potential of these systems for application to drug delivery, we focused our attention on determining their encapsulation efficiency and release profiles. We measured encapsulation efficiencies over 85% and a 100% release that can be tuned from 20 to 300 min depending on the selected phase. In general, we believe that the here reported ternary diagrams can be used to design new biocomposites with tailored functional properties for bio-catalysis, bio-banking and drug delivery. As a proof of concept, we applied the ternary diagram to synthesize insulin bio-composites and test their encapsulation and release properties. Finally, we uncovered for the first time proteins@**ZIF-C** composites. For BSA@**ZIF-C** and insulin@**ZIF-C**, we measured $\text{EE}_{\text{BSA}} = 99\%$ and $\text{EE}_{\text{insulin}} = 94\%$, and 100% release was achieved in 120 and 200 min, respectively. This new bioMOF composite is an appealing crystalline structure alternative to **sod** and **dia** with potentially useful properties for encapsulation and release of biotherapeutics.

Conflicts of interest

There are no conflicts to declare.

Acknowledgements

The research leading to these results has received funding from the European Research Council under the European Union's Horizon 2020 Programme (FP/2014-2020)/ERC Grant Agreement no. 771834 – POPCRYSTAL. The authors acknowledge support from the European Union's Horizon 2020 FETOPEN-1-2016-2017 research and innovation program under grant agreement 801464. This work was supported by the Australian Research Council Discovery Project (DP170103531). P. F. acknowledges TU Graz for the Lead Project (LP-03). M. J. V. H. acknowledges The National Council of Science and Technology (CONACyT, México) for the postdoctoral scholarship (CVU 419210). R. R. acknowledges the European Union's Horizon 2020 research and innovation programme under the Marie Skłodowska-Curie grant agreement #748649 (project "MNEMONIC"). Financial support from the Swedish Research Council (2017-0432) and the Knut and Alice Wallenberg Foundation (KAW 2016.0072) are gratefully acknowledged.

Notes and references

- H. Furukawa, K. E. Cordova, M. O'Keeffe and O. M. Yaghi, *Science*, 2013, **341**, 1230444.
- A. C. McKinlay, R. E. Morris, P. Horcajada, G. Férey, R. Gref, P. Couvreur and C. Serre, *Angewandte Chemie International Edition*, 2010, **49**, 6260–6266.
- P. Horcajada, C. Serre, M. Vallet-Regí, M. Sebban, F. Taulelle and G. Férey, *Angewandte Chemie International Edition*, 2006, **45**, 5974–5978.
- S. Wuttke, A. Zimpel, T. Bein, S. Braig, K. Stoiber, A. Vollmar, D. Müller, K. Haastert-Talini, J. Schaeske, M. Stiesch, G. Zahn, A. Mohmeyer, P. Behrens, O. Eickelberg, D. A. Bölükbas and S. Meiners, *Advanced Healthcare Materials*, 2017, **6**, 1600818.
- C. Doonan, R. Riccò, K. Liang, D. Bradshaw and P. Falcaro, *Accounts of Chemical Research*, 2017, **50**, 1423–1432.
- D. A. LaVan, D. M. Lynn and R. Langer, *Nat Rev Drug Discov*, 2002, **1**, 77–84.
- Y. Chen, P. Li, J. A. Modica, R. J. Drout and O. K. Farha, *J. Am. Chem. Soc.*, 2018, **140**, 5678–5681.
- Y. Feng, H. Wang, S. Zhang, Y. Zhao, J. Gao, Y. Zheng, P. Zhao, Z. Zhang, M. J. Zaworotko, P. Cheng, S. Ma and Y. Chen, *Advanced Materials*, 2019, **31**, 1805148.
- J. Yao and H. Wang, *Chem. Soc. Rev.*, 2014, **43**, 4470–4493.
- B. Chen, Z. Yang, Y. Zhu and Y. Xia, *J. Mater. Chem. A*, 2014, **2**, 16811–16831.
- K. Liang, R. Ricco, C. M. Doherty, M. J. Styles, S. Bell, N. Kirby, S. Mudie, D. Haylock, A. J. Hill, C. J. Doonan and P. Falcaro, *Nature Communications*, DOI:10.1038/ncomms8240.
- W. Liang, H. Xu, F. Carraro, N. K. Maddigan, Q. Li, S. G. Bell, D. M. Huang, A. Tarzia, M. B. Solomon, H. Amenitsch, L. Vaccari, C. J. Sumby, P. Falcaro and C. J. Doonan, *Journal of the American Chemical Society*, 2019, **141**, 2348–2355.
- F. Lyu, Y. Zhang, R. N. Zare, J. Ge and Z. Liu, *Nano Lett.*, 2014, **14**, 5761–5765.
- X. Wu, M. Hou and J. Ge, *Catalysis Science & Technology*, 2015, **5**, 5077–5085.
- X. Wu, J. Ge, C. Yang, M. Hou and Z. Liu, *Chemical Communications*, 2015, **51**, 13408–13411.
- F.-K. Shieh, S.-C. Wang, C.-I. Yen, C.-C. Wu, S. Dutta, L.-Y. Chou, J. V. Morabito, P. Hu, M.-H. Hsu, K. C.-W. Wu and C.-K. Tsung, *J. Am. Chem. Soc.*, 2015, **137**, 4276–4279.
- N. K. Maddigan, A. Tarzia, D. M. Huang, C. J. Sumby, S. G. Bell, P. Falcaro and Christian. J. Doonan, *Chemical Science*, 2018, **9**, 4217–4223.
- E. Astria, M. Thonhofer, R. Ricco, W. Liang, A. Chemelli, A. Tarzia, K. Alt, C. E. Hagemeyer, J. Rattenberger, H. Schroettner, T. Wrodnigg, H. Amenitsch, D. M. Huang, C. J. Doonan and P. Falcaro, *Materials Horizons*, 2019, 10.1039.C8MH01611A.
- S. Li, M. Dharmawardana, R. P. Welch, C. E. Benjamin, A. M. Shamir, S. O. Nielsen and J. J. Gassensmith, *ACS Appl. Mater. Interfaces*, 2018, **10**, 18161–18169.
- M. Hoop, C. F. Walde, R. Riccò, F. Mushtaq, A. Terzopoulou, X.-Z. Chen, A. J. deMello, C. J. Doonan, P. Falcaro, B. J. Nelson, J. Puigmartí-Luis and S. Pané, *Applied Materials Today*, 2018, **11**, 13–21.
- T.-T. Chen, J.-T. Yi, Y.-Y. Zhao and X. Chu, *Journal of the American Chemical Society*, 2018, **140**, 9912–9920.
- W. Chen and C. Wu, *Dalton Trans.*, 2018, **47**, 2114–2133.
- X. Wu, C. Yang and J. Ge, *Bioresources and Bioprocessing*, 2017, **4**, 24.
- M. de J. Velásquez-Hernández, R. Ricco, F. Carraro, F. T. Limpoco, M. Linares-Moreau, E. Leitner, H. Wiltse, J. Rattenberger, H. Schröttner, P. Frühwirth, E. M. Stadler, G. Gescheidt, H. Amenitsch, C. J. Doonan and P. Falcaro, *CrystEngComm*, 2019, **21**, 4538–4544.
- M. A. Luzuriaga, C. E. Benjamin, M. W. Gaertner, H. Lee, F. C. Herbert, S. Mallick and J. J. Gassensmith, *Supramolecular Chemistry*, 2019, **0**, 1–6.
- O. Karagiari, M. B. Lalonde, W. Bury, A. A. Sarjeant, O. K. Farha and J. T. Hupp, *J. Am. Chem. Soc.*, 2012, **134**, 18790–18796.
- Q. Bao, Y. Lou, T. Xing and J. Chen, *Inorganic Chemistry Communications*, 2013, **37**, 170–173.
- K. Kida, M. Okita, K. Fujita, S. Tanaka and Y. Miyake, *CrystEngComm*, 2013, **15**, 1794.
- M. Jian, B. Liu, R. Liu, J. Qu, H. Wang and X. Zhang, *RSC Advances*, 2015, **5**, 48433–48441.
- A. D. Katsenis, A. Puškarić, V. Štrukil, C. Mottillo, P. A. Julien, K. Užarević, M.-H. Pham, T.-O. Do, S. A. J. Kimber, P. Lazić, O. Magdysyuk, R. E. Dinnebier, I. Halasz and T. Friščić, *Nature Communications*, 2015, **6**, 6662.
- M. He, J. Yao, Q. Liu, K. Wang, F. Chen and H. Wang, *Microporous and Mesoporous Materials*, 2014, **184**, 55–60.
- Z. Akimbekov, A. D. Katsenis, G. P. Nagabhushana, G. Ayoub, M. Arhangelskis, A. J. Morris, T. Friščić and A. Navrotsky, *J. Am. Chem. Soc.*, 2017, **139**, 7952–7957.
- R. Chen, J. Yao, Q. Gu, S. Smeets, C. Baerlocher, H. Gu, D. Zhu, W. Morris, O. M. Yaghi and H. Wang, *Chemical Communications*, 2013, **49**, 9500–9502.
- W. Liang, R. Ricco, N. K. Maddigan, R. P. Dickinson, H. Xu, Q. Li, C. J. Sumby, S. G. Bell, P. Falcaro and C. J. Doonan, *Chemistry of Materials*, 2018, **30**, 1069–1077.
- S. Cao, T. D. Bennett, D. A. Keen, A. L. Goodwin and A. K. Cheetham, *Chem. Commun.*, 2012, **48**, 7805–7807.
- C. Avci, J. Ariñez-Soriano, A. Carné-Sánchez, V. Guillermin, C. Carbonell, I. Imaz and D. Maspoch, *Angewandte Chemie International Edition*, 2015, **54**, 14417–14421.
- D. J. Connell, A. Gebril, M. A. H. Khan, S. V. Patwardhan, K. Kubiak-Ossowska, V. A. Ferro and P. A. Mulheran, *Scientific Reports*, 2018, **8**, 17115.
- K. A. Majorek, P. J. Porebski, A. Dayal, M. D. Zimmerman, K. Jablonska, A. J. Stewart, M. Chruszcz and W. Minor, *Mol Immunol*, 2012, **52**, 174–182.
- W. Liang, F. Carraro, M. B. Solomon, S. G. Bell, H. Amenitsch, C. J. Sumby, N. G. White, P. Falcaro and C. J. Doonan, *J. Am. Chem. Soc.*, 2019, **141**, 14298–14305.
- S. A. Basnayake, J. Su, X. Zou and K. J. Balkus, *Inorg. Chem.*, 2015, **54**, 1816–1821.
- M. O. Cichocka, J. Ångström, B. Wang, X. Zou and S. Smeets, *J Appl Crystallogr*, 2018, **51**, 1652–1661.
- S. Yuan, J.-S. Qin, H.-Q. Xu, J. Su, D. Rossi, Y. Chen, L. Zhang, C. Lollar, Q. Wang, H.-L. Jiang, D. H. Son, H. Xu, Z. Huang, X. Zou and H.-C. Zhou, *ACS Cent. Sci.*, 2018, **4**, 105–111.
- Y. Lo, C. H. Lam, C.-W. Chang, A.-C. Yang and D.-Y. Kang, *RSC Advances*, 2016, **6**, 89148–89156.
- L. Bouëssel du Bourg, A. U. Ortiz, A. Boutin and F.-X. Coudert, *APL Materials*, 2014, **2**, 124110.
- M. Baker, *Nat Biotechnol*, 2005, **23**, 1065–1072.
- T. W. Overton, *Drug Discovery Today*, 2014, **19**, 590–601.
- G. Walsh, *Nat Biotechnol*, 2010, **28**, 917–924.
- W. Chang, J. Cheng, J. J. Allaire, Y. Xie, J. McPherson, RStudio, jQuery F. (jQuery library and jQuery U. library), jQuery contributors (jQuery library; authors listed in

- inst/www/shared/jquery-AUTHORS.txt), jQuery U. contributors (jQuery U. library; authors listed in inst/www/shared/jqueryui/AUTHORS.txt), M. O. (Bootstrap library), J. T. (Bootstrap library), B. contributors (Bootstrap library), Twitter, I. (Bootstrap library), A. F. (html5shiv library), S. J. (Respond js library), S. P. (Bootstrap-datepicker library), A. R. (Bootstrap-datepicker library), D. G. (Font-A. font), B. R. (selectize js library), K. M. K. (es5-shim library), es5-shim contributors (es5-shim library), D. I. (ion rangeSlider library), S. S. (Javascript strftime library), S. L. (DataTables library), J. F. (showdown js library), J. G. (showdown js library), I. S. (highlight js library) and R. C. T. (tar implementation from R), *shiny: Web Application Framework for R*, 2019.
- 49 A. Barth, *Biochimica et Biophysica Acta (BBA) - Bioenergetics*, 2007, **1767**, 1073–1101.
 - 50 M. Jackson and H. H. Mantsch, *Critical Reviews in Biochemistry and Molecular Biology*, 1995, **30**, 95–120.
 - 51 Y. Hu, H. Kazemian, S. Rohani, Y. Huang and Y. Song, *Chem. Commun.*, 2011, **47**, 12694–12696.
 - 52 G. Kumari, K. Jayaramulu, T. K. Maji and C. Narayana, *J. Phys. Chem. A*, 2013, **117**, 11006–11012.
 - 53 J. Ethiraj, F. Bonino, C. Lamberti and S. Bordiga, *Microporous and Mesoporous Materials*, 2015, **207**, 90–94.
 - 54 G. Socrates, *Infrared and Raman Characteristic Group Frequencies: Tables and Charts*, John Wiley & Sons, 2004.
 - 55 N. Kuhar, S. Sil, T. Verma and S. Umapathy, *RSC Adv.*, 2018, **8**, 25888–25908.
 - 56 M. Wang, L. Jiang, E. J. Kim and S. H. Hahn, *RSC Adv.*, 2015, **5**, 87496–87503.
 - 57 C. Li, L. Xing and S. Che, *Dalton Trans.*, 2012, **41**, 3714–3719.
 - 58 H. Qing, H. Yanlin, S. Fenlin and T. Zuyi, *Spectrochimica Acta Part A: Molecular and Biomolecular Spectroscopy*, 1996, **52**, 1795–1800.
 - 59 A. S. Determan, B. G. Trewyn, V. S.-Y. Lin, M. Nilsen-Hamilton and B. Narasimhan, *Journal of Controlled Release*, 2004, **100**, 97–109.
 - 60 K. N. Clayton, D. Lee, S. T. Wereley and T. L. Kinzer-Ursem, *Lab Chip*, 2017, **17**, 4148–4159.
 - 61 M. Mishra, *Handbook of Encapsulation and Controlled Release*, CRC Press, 2015.
 - 62 M. L. Hans and A. M. Lowman, *Current Opinion in Solid State and Materials Science*, 2002, **6**, 319–327.
 - 63 C.-Y. Sun, C. Qin, X.-L. Wang and Z.-M. Su, *Expert Opinion on Drug Delivery*, 2013, **10**, 89–101.
 - 64 F. O. Costa, J. J. S. Sousa, A. A. C. C. Pais and S. J. Formosinho, *Journal of Controlled Release*, 2003, **89**, 199–212.
 - 65 K. Zhang, R. P. Lively, C. Zhang, R. R. Chance, W. J. Koros, D. S. Sholl and S. Nair, *J. Phys. Chem. Lett.*, 2013, **4**, 3618–3622.
 - 66 K. Ghosal, A. Chandra, R. Rajabalaya, S. Chakraborty and A. Nanda, *Pharmazie*, 2012, **67**(2), 147–55.

TOC

